Editors' Suggestion

Topological Field-Effect Transistor Based on Quasi-Two-Dimensional Tellurium Flakes

Bin Cheng,[1,2] Lin Li,[1,2,*] Nan Zhang,[1,2] Ling Zhang,[1,2] Xianglin Li,[1,2] Zhiyong Lin,[1,2] Hui Li,[3] Zhengfei Wang,[2] and Changgan Zeng[1,2,†]

[1] *CAS Key Laboratory of Strongly-Coupled Quantum Matter Physics, and Department of Physics, University of Science and Technology of China, Hefei, Anhui 230026, China*

[2] *International Center for Quantum Design of Functional Materials (ICQD), and Synergetic Innovation Center of Quantum Information and Quantum Physics, University of Science and Technology of China, Hefei, Anhui 230026, China*

[3] *Institutes of Physical Science and Information Technology, Anhui University, Hefei, Anhui 230601, China*

(Received 13 February 2022; accepted 28 April 2022; published 26 May 2022)

For semiconductors, adding a degree of freedom beyond charge, e.g., spin and valley, will lead to alternative physics and device applications. Here, we demonstrate that another electronic degree of freedom, the chirality of Weyl node, can be used in the Weyl semiconductor tellurium, a unique system harnessing intriguing Weyl physics and high tunability of the semiconductor. By constructing a field-effect device based on quasi-two-dimensional tellurium flakes, the Fermi level can be effectively tuned from the top of valence bands, where the Weyl nodes locate at, into the bandgap via electrostatic gating. In addition to a significant reduction of channel conductivity, a transition from chiral-anomaly-induced negative magnetoresistance to conventional positive magnetoresistance occurs at the same time, indicating complete suppression of the chirality-related topological transport. The simultaneous switch of both conducting and topological states is unprecedented in previous Weyl semimetals. Our findings pave the way for developing new-principle semiconductor devices with fascinating functionalities.

DOI: 10.1103/PhysRevApplied.17.054044

I. INTRODUCTION

For semiconductor devices serving as key elements for the majority of electronic systems, the gradual coming of the "end of Moore's law" has renewed research and industry efforts, from miniaturization of long-established technologies to the exploration of innovative materials and nanodevice architectures. A representative example is the rise of semiconductor spintronics, where the spin degree of freedom is further utilized to develop hybrid devices that can perform various operations like logic, communications, and storage, with low power consumption and fast operation [1,2]. Similarly, much effort has been made to manipulate the electronic valley degree of freedom to encode and process information, especially in recent two-dimensional (2D) semiconductors like transition metal dichalcogenides [3,4].

On the other hand, the emergent different categories of topological materials have received considerable attention for developing new-principle devices, mainly due to their novel topological electronic properties with high robustness against external perturbations. Among them, Weyl semimetals hosting quasiparticles known as Weyl fermions are of particular interest [5,6]. In Weyl systems, crossings of nondegenerate linearly dispersive bands constitute the Weyl nodes, which behave as the source (monopole) or sink (antimonopole) of Berry curvature in momentum space [7]. The chirality of the Weyl node, which is given by the sign of the corresponding monopole charge, acts as a brand-new electronic degree of freedom, and dominates many exotic transport phenomena, such as chiral-anomaly-induced unique magnetotransport behaviors [8–11] and the giant photovoltaic effect originating from the optical selection rules of Weyl nodes [12,13]. However, in these semimetals, the lack of tunability greatly hinders effective manipulation of chirality-related topological transport properties.

Fortunately, recent studies have demonstrated that Weyl physics can also be achieved in an elemental semiconductor tellurium (Te) [14–18], endowing conventional semiconductors with chirality degree of freedom. For such a type of Weyl material, referred to as a "Weyl semiconductor" [14], Weyl band crossing exists in the top of valence bands and/or the bottom of conduction bands. Even though a Weyl semiconductor is actually rooted in the same nontrivial band topology as that in a Weyl semimetal [Fig. 1(a)], the existence of a bandgap leads to the strong

*Corresponding author. lilin@ustc.edu.cn
†Corresponding author. cgzeng@ustc.edu.cn

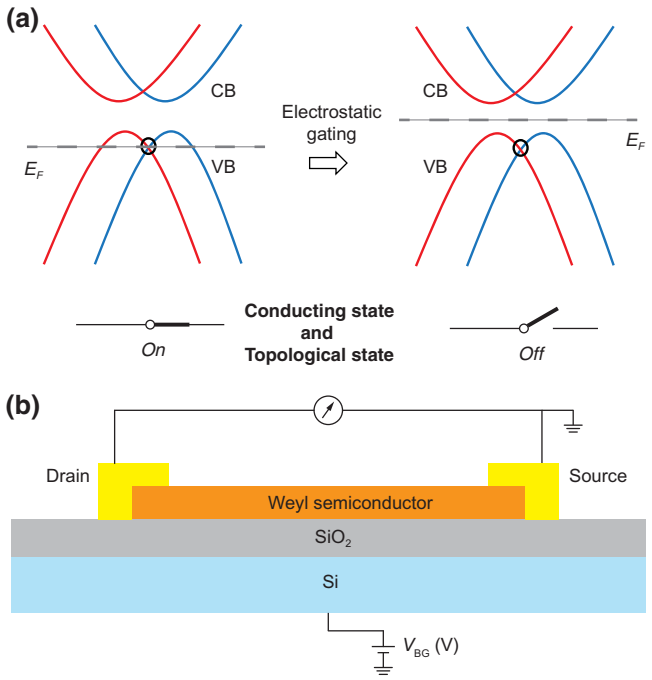

FIG. 1. Topological field-effect transistor based on the Weyl semiconductor.(a) Schematic illustration of the tuning effect on a Weyl semiconductor via electrostatic gating, in which the Weyl node is marked by the black circle. Here a simplified schematic of the band structure is shown, aiming to capture the key features of a more general class of Weyl semiconductor, i.e., band crossing with twofold degeneracy in the top of valence bands and/or the bottom of conduction bands. Left panel: the Fermi level is located in the valence bands (VBs) and near the Weyl node, corresponding to the *on* state for both the channel conductivity and chirality-related topological transport. Right panel: applying electrostatic gating shifts the Fermi level into the bandgap, leading to the simultaneous switch off of the conducting and topological states. (b) Schematic of the field-effect device based on the Weyl semiconductor. Electrostatic tuning of the Fermi level is achieved via applying a back-gate voltage (V_{BG}) using SiO_2 as the dielectric layer.

coupling of charge transport and chirality-related topological transport, making it a better platform to manipulate the chirality degree of freedom in addition to the charge one. This feature can be further utilized to realize novel topological devices, like the promising topological field-effect transistor (TFET) in which the conducting and topological states can be switched on and off simultaneously (as conceptually presented in Fig. 1).

II. RESULTS

Te is a narrow bandgap semiconductor with a unique one-dimensional van der Waals structure [Fig. 2(a)] [15,19]. Figure 2(a) also shows the calculated band structures along the *L*-*H*-*K* line, from which a Weyl node located at about 0.2 eV below the top of valence bands (VBs) is seen (for more details of calculated band structures of Te, see Fig. S1 of the Supplemental Material [20]). As previously demonstrated, the naturally hole-doping character of the Te bulk crystal prompts the Fermi level to cross the Weyl bands, which guarantees relatively large Berry curvature at the Fermi level and thus the emergence of various magnetotransport signatures of Weyl physics [14]. On the other hand, (quasi-)2D Te can be prepared via different routes, like physical vapor deposition [21] and hydrothermal methods [22,23]. Such an easily obtained low-dimensional Weyl semiconductor is thus an ideal candidate for realizing the aforementioned TFET device.

In this study, the hydrothermal method is adopted to grow Te with a quasi-2D structure. Figure 2(b) shows the optical image of the grown Te flakes with characteristic trapezoid shapes, and the typical thickness ranges from 20 to 100 nm. High-resolution transmission electron microscopy images and the selective area diffraction pattern show that the Te flake is of high single-crystalline quality, and the long axis is oriented along the [0001] direction [see Figs. S2(c) and S2(d) of the Supplemental Material [20]]. Figure 2(c) shows the temperature- (T) dependent resistance (R) curve of Te flake device no. 1 (thickness about 27 nm) fabricated on the SiO_2/Si substrate, with the current applied along the [0001] direction. As the temperature decreases, R decreases first and then increases continuously, with a minimum occurring at $T \sim$ 25 K, behavior typical of the *R*-*T* features of a doped semiconductor. Hall measurements at varied temperatures demonstrate that the Te flake is also naturally hole-doping [see the Hall data in Fig. S3(a) of the Supplemental Material [20]], and the extracted carrier density shows a steady increase with increasing temperature [left upper inset of Fig. 2(c)]. In contrast, the corresponding carrier mobility gets significantly decreased with increasing temperature, which can be attributed to enhanced electron-phonon scattering [24]. Notably, the mobility at temperatures up to 300 K still remains above 400 $cm^2V^{-1}s^{-1}$, indicating the superiority of the Te flake as the 2D channel material of FETs.

Figure 2(d) shows the MR curves measured at 1.5 K. When the magnetic field (B) is perpendicular to the current (I), conventional positive MR behavior is obtained throughout the measured field range, except for the small negative MR around the zero field. As presented in the inset, such a low-field correction can be well fit by the Hikami-Larkin-Nagaoka (HLN) equation [25], indicating the emergence of the weak localization effect (as detailed in Sec. 2 of the Supplemental Material [20]). For the case of $B||I$, nonsaturated negative MR is clearly seen, consistent with the key signature of chiral anomaly that has been widely observed in Weyl systems [9,26–29]. Here, the chiral anomaly refers to the density imbalance of chiral charges, which is induced by the pumping of Weyl

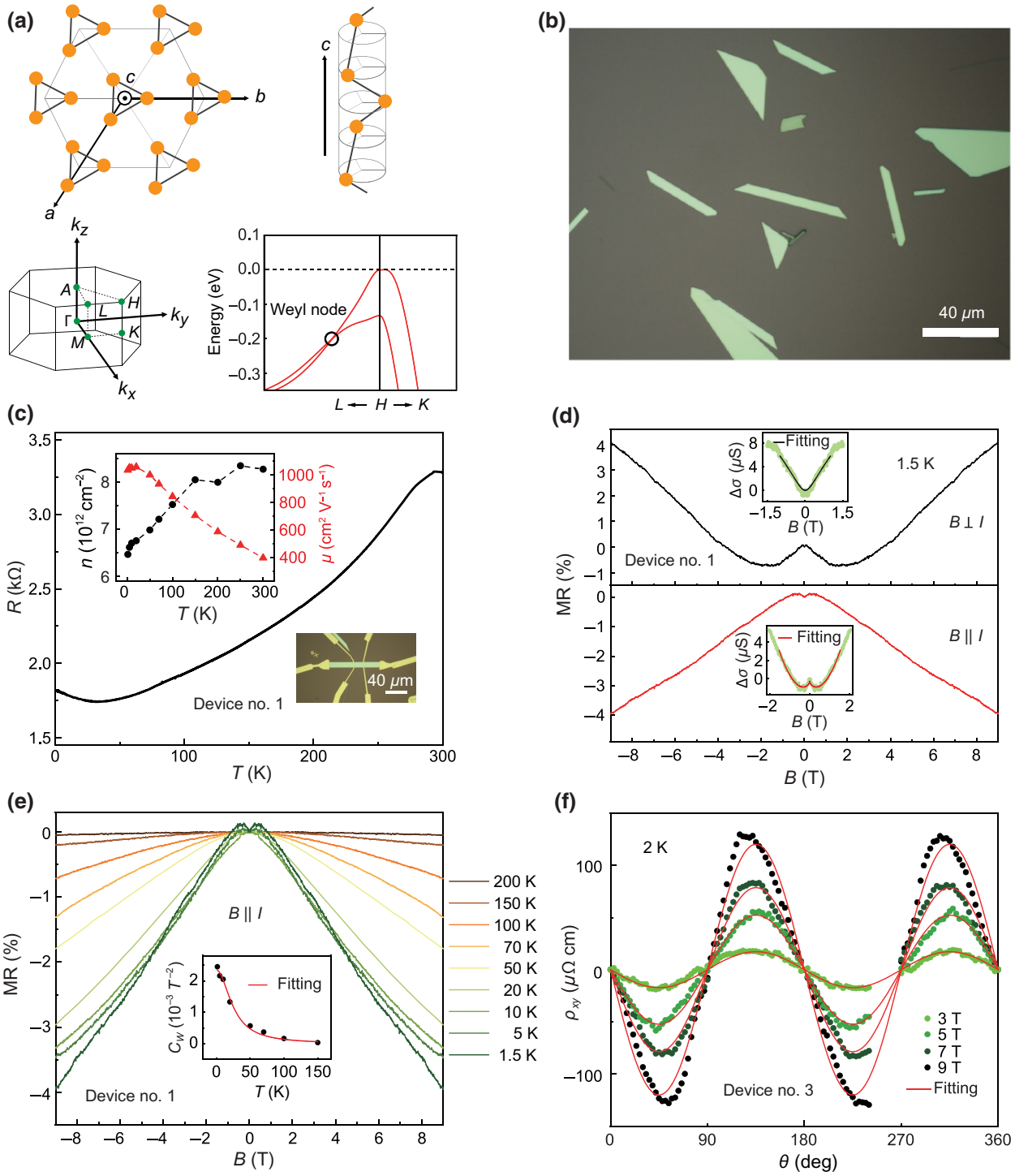

FIG. 2. Basic transport characterizations. (a) Top: top and perspective views of the crystal structure of Te. Bottom: Brillouin zone of trigonal Te and calculated energy dispersion of electronic bands along the *L*-*H*-*K* line with spin-orbit coupling. The Weyl node located near the top of the VBs is marked by a black circle. (b) Optical image of Te flakes deposited on a SiO_2/Si substrate. (c) Temperature-dependent resistance of Te flake device no. 1. Left upper inset: temperature-dependent carrier density and mobility. Right lower inset: optical image of the device. (d) Magnetoresistance (MR) at 1.5 K with magnetic field (B) perpendicular and parallel to the current (I). Inset in the upper panel: low-field fitting of the magnetoconductivity for $B \perp I$ using the HLN equation. Inset in the lower panel: low-field fitting of the magnetoconductivity for $B||I$ using Eq. (1), from which the chiral coefficient C_W can be extracted. (e) MR curves for $B||I$ measured at varied temperatures up to 200 K. Inset: the extracted C_W as a function of temperature, which can be well fit via Eq. (2). (f) In-plane angular-dependent planar Hall resistivity of device no. 3 measured at 2 K for various magnetic fields and corresponding fittings using Eq. (S2) in the Supplemental Material [20].

fermions from one Weyl node to another with opposite chirality under the parallel electric and magnetic fields [27]. This pumping process leads to a net chiral current that is nondissipative even in the presence of strong external perturbations [30,31], and contributes an extra conductivity component in addition to the Ohmic one, manifested as the negative longitudinal MR that is rare in nonferromagnetic materials. For quantitatively validating this picture, we then fit the $B||I$ data using the following equation of chiral-anomaly-induced magnetoconductivity [9]:

$$\sigma(B) = (1 + C_W B^2)\sigma_{\mathrm{WAL}} + \sigma_N. \tag{1}$$

Here C_W is the chiral coefficient representing the strength of the chiral-anomaly effect, σ_{WAL} and σ_N are the conductivities contributed by the weak antilocalization effect and conventional nonlinear band around the Fermi surface, respectively. Here, $\sigma_{\mathrm{WAL}} = \sigma_0 + a\sqrt{B}$, $\sigma_N^{-1} = \rho_0 + A \times B^2$, and σ_0 is zero-field conductivity. As demonstrated in the inset of Fig. 2(d), the experimental data can be well fit with Eq. (1). With increasing temperature, the negative MR gradually degrades due to thermal effects and becomes negligible at $T = 200$ K [see Fig. 2(e) and the corresponding fitting results in Fig. S5 of the Supplemental Material [20]]. The extracted values of C_W at different temperatures can be further fit by the theoretically expected equation depicting the evolution behavior of chiral coefficient [31] [see the inset of Fig. 2(e)]:

$$C_W \propto \frac{v_F^3 \tau_v}{T^2 + \mu_W^2/\pi^2}. \tag{2}$$

Here v_F is the Fermi velocity, τ_v is the chirality-changing scattering time, and μ_W is the chemical potential relative to the Weyl node. All these analyses point to the chiral-anomaly origin of the observed negative MR under parallel magnetic field in Te flakes. This result, together with the observed planar Hall effect shown in Fig. 2(f) (see Sec. 4 of the Supplemental Material for the details [20]), demonstrates that Te flakes also possess Weyl physics, identical to the case of bulk crystals. After further ruling out other possible origins (see more discussions in Sec. 3 of the Supplemental Material [20]), such a negative longitudinal MR behavior acts as a fingerprint signature for the existence of chiral anomaly, and is thus indicative of the topological state.

Below, we investigate the field-effect performance of our Te flake device. Figure 3(a) shows the transfer curves of device no. 1 measured under different source-drain voltages (V_{SD}). Taking the 10 mV data as an example, when sweeping the back-gate voltage (V_{BG}) from -60 to 50 V at 1.5 K, the measured I_{SD} decreases from 2.3 to 7.0×10^{-3} μA, corresponding to an on-off current ratio of about 3×10^2. This switch characteristic demonstrates the effective modulation of the Fermi level from the top of VBs into the bandgap. When further increasing V_{BG} from 50 V, a slight increase of I_{SD} is observed, indicating that the Fermi level is further shifted towards the conduction bands. The high tunability of the charge transport can be further demonstrated from the evident change of carrier density with varying V_{BG} measured at the hole side [see the Hall data in Fig. S3(b) of the Supplemental Material [20]]. As shown in Fig. 3(b), when V_{BG} increases from -60 to 40 V, the carrier density decreases monotonically from 1.4×10^{13} to 4×10^{12} cm^{-2}. Nevertheless, the corresponding carrier mobility maintains a magnitude of about 1000 cm^{2}V^{-1}s^{-1} within a wide V_{BG} range of -60 to 10 V. A rapid decrease of mobility only occurs at $V_{\mathrm{BG}} > 10$ V, which may result from the degraded screening effect on charged impurity scattering due to reduced carrier density [32,33].

We further measured the I_{SD}-V_{SD} curves under different V_{BG}, and the typical results are shown in Fig. 3(c). It is clear that the I_{SD}-V_{SD} curves remain linear when varying V_{BG} from -60 to 20 V, indicating good Ohmic contact at the hole side. When applying a relatively high positive V_{BG}, e.g., in the range of 30–60 V, the I_{SD}-V_{SD} curves become nonlinear [inset of Fig. 3(c)], which should be caused by the formation of a Schottky barrier at the interface due to the work function mismatch between the Te flake and metal electrodes.

As mentioned above, for Weyl materials like Te, the negative MR under parallel B is actually rooted in the generation of an extra chiral current in addition to the conventional Ohmic one. Such a chiral current can be depicted using the equation [31]

$$\mathbf{J}_{\mathrm{chiral}} = \frac{e^2}{2\pi^2}\mu_5 \mathbf{B}, \tag{3}$$

where μ_5 is the chemical potential difference between the two kinds of Weyl nodes with opposite chiralities, which can be described as

$$\mu_5 = \frac{3}{4}\frac{v_F^3}{\pi^2}\frac{e^2}{\hbar^2 c}\tau_v \frac{\mathbf{E} \times \mathbf{B}}{T^2 + \mu_W^2/\pi^2}. \tag{4}$$

That is, the chiral anomaly effect can also be manifested as the increasing of I_{SD} in response to B when using the same two-probe configuration as that of the I_{SD}-V_{SD} measurements. This is indeed what we have observed when $V_{\mathrm{BG}} = 0$ V [Fig. 3(d)], at which the Fermi level is located near the Weyl node within the VBs. After increasing V_{BG} to 20 V, the magnitude of increment of I_{SD} (ΔI_{SD}) decreases obviously. This is due to the fact that the positive V_{BG} leads to an upshift of the Fermi level and thus the increased distance between the Fermi level and the Weyl node, i.e., larger μ_W in Eq. (4). When the applied V_{BG} is high enough to shift the Fermi level into the bandgap, e.g., above 50 V, ΔI_{SD} becomes negligible or even negative with increasing B, demonstrating complete suppression of the chiral

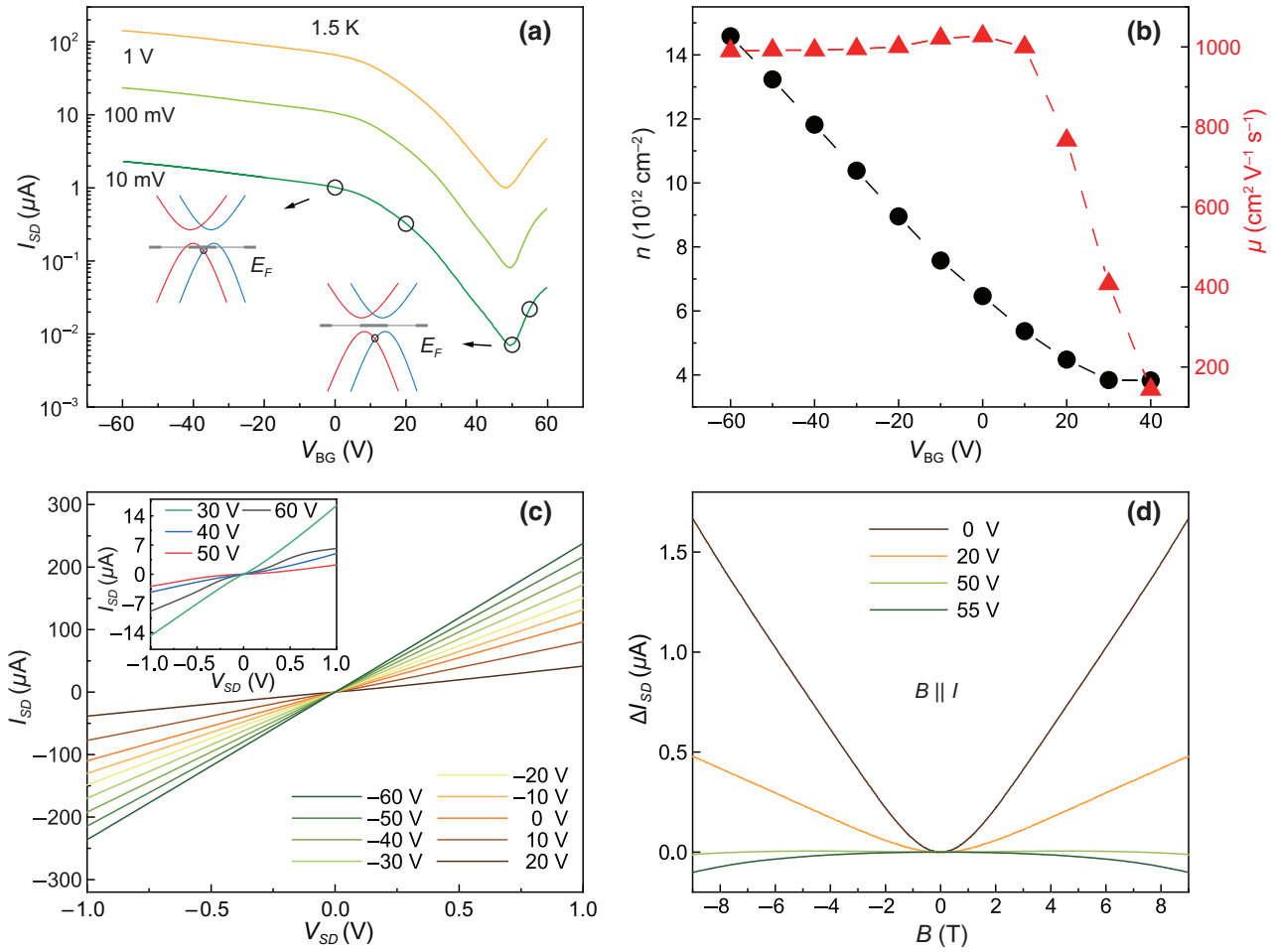

FIG. 3. Field-effect performance. (a) Semilog plot of the source-drain current (I_{SD}) as a function of V_{BG} measured at three typical source-drain voltages (V_{SD}) for Te flake device no. 1. Schematics of the position of the Fermi level for representative V_{BG} are also shown in the inset. (b) The extracted carrier density and mobility at 1.5 K for different V_{BG}. (c) The source-drain current I_{SD} as a function of V_{SD} measured at 1.5 K. Linear behavior is observed for varied V_{BG} from −60 to 20 V. Inset: nonlinear I_{SD}-V_{SD} curves obtained at relatively high positive V_{BG}. (d) The increment of I_{SD} as a function of B for $B||I$ at several representative V_{BG} [marked by black circles in (a)]. The source-drain voltage V_{SD} is set to be 0.5 V during the measurements.

anomaly. Therefore, accompanying the switch of channel conductivity, the switch of chirality-related topological transport can also be readily achieved in the present Te-based field-effect device, both of which rely on the shift of the Fermi level from the VBs into the bandgap.

To better demonstrate the dual-tuning effect of the charge and chirality transport, more detailed measurements of the field-effect performance are conducted using a four-probe configuration. Figure 4(a) shows the resistance of device no. 2 as a function of V_{BG} measured at 1.5 K. When increasing V_{BG} from −80 V, the resistance increases first and then decreases, consistent with the am-bipolar character observed in device no. 1 [see the I_{SD}-V_{BG} data shown in Fig. 3(a)]. The resistance peak occurs at $V_{BG} \sim 60$ V, with the corresponding value about three magnitudes larger than that at $V_{BG} = -80$ V, corresponding to a significant change in channel conductivity. Meanwhile, the effective switch of chirality transport is also achieved when the applied V_{BG} is high enough to move the Fermi level into the bandgap, as shown in Fig. 4(b) and Fig. S7 of the Supplemental Material [20]. Taking the 1.5 K data as an example, for pristine Te flakes without electrostatic gating, a clear chiral-anomaly-induced negative MR behavior under parallel B is seen. This effect is significantly suppressed when a positive V_{BG} like 40 V is applied. If V_{BG} is increased further, conventional positive MR instead of negative MR is obtained, indicating the breakdown of the chiral anomaly effect. Figures 4(c) and 4(d) further show the mappings of resistance and MR as functions of V_{BG} and B. It is clear that the remarkable increase of resistance is accompanied by the transition from negative to positive MR, well demonstrating the simultaneous switch of conducting and topological states in our Te device (see Fig. S8 of the Supplemental Material [20] for similar

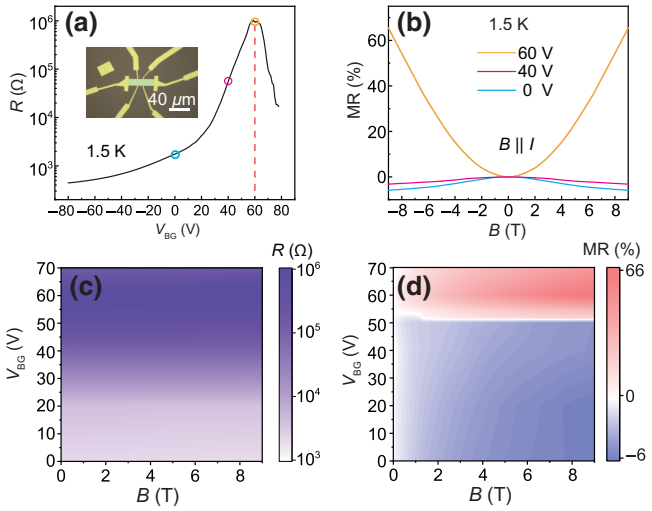

FIG. 4. Dual-switch of charge and chirality transport. (a) Semilog plot of R versus V_{BG} for Te flake device no. 2. (b) MR curves for $B||I$ at several representative V_{BG} [marked by circles in (a)] measured at 1.5 K. (c) The resistance R versus (V_{BG}, B) obtained at 1.5 K. (d) MR versus (V_{BG}, B) obtained at 1.5 K.

results for device no. 4). Within the range of measurement parameters, the resistance change is more than 3 orders of magnitude and the MR change is higher than 70%, exhibiting high tunability for both of them. Further optimizing the device, e.g., using a thinner Te flake sample and/or a high-κ dielectric layer, is expected to achieve a more prominent field-effect performance.

It is well known that in conventional FETs, only the charge degree of freedom is fully utilized, and the modulation of channel conductivity is realized by injecting or depleting free carriers via electrostatic gating. The concept of "TFET" has actually been previously proposed accompanying the deep understanding of topological electronic properties of emerging topological materials [34–37]. One typical example is based on the quantum spin Hall insulator [35], where the presence or absence of dissipationless edge channels determines the on or off state of channel conductivity. Such a proposal relies on the phase transition from topological insulator to ordinary insulator by applying an ultralarge vertical electric field, which, however, is not accessible when using a conventional FET configuration. Therefore, only spectroscopic evidence obtained by scanning tunneling microscopy has been presented up to now [38].

In sharp contrast, for the present TFET based on Te flakes, chirality-related topological transport can be effectively modified at the same time as the charge-based channel conductivity. Such a combined functionality is readily achieved by applying a moderate back-gate voltage in a standard FET configuration, without complicated fabrication or operation processes. Note that here the *on* (*off*) state for the Te-based TFET refers to the strongly coupled high (low) channel conductivity and negative (positive) longitudinal MR. The as-revealed high sensitivity of channel current to both electric and magnetic fields makes Te a promising candidate for building hybrid devices with multifield control. The simultaneous switch of both conducting and topological states, to the best of our knowledge, is unprecedented in widely studied Weyl semimetals. Note that the induced chiral current under parallel magnetic field arises from the unique chiral anomaly effect of Weyl systems, and is theoretically predicted to be topologically protected against perturbations like back scattering and disorder [39]. The successful achievement of its high tunability in a semiconductor system sheds light on developing low-consumption devices compatible with the modern electronic industry.

III. CONCLUSIONS

In summary, based on the Weyl semiconductor Te, we successfully developed a type of TFET in which channel conductivity and chirality-related topological transport can be simultaneously switched via electrostatic control. This achievement benefits from the introduction of a unique chirality degree of freedom into the semiconductor system that possesses high electronic tunability. Note that, in addition to the chiral-anomaly-induced magnetotransport features that we focus on in the present study, many other intriguing chirality-related electronic properties have also been revealed in Weyl systems, such as the circular photogalvanic effect [12,13], the discrete scale invariance [14,40], and the anomalous Hall effect [29,41,42]. Further exploiting and manipulating these properties will be quite promising in a Weyl semiconductor, providing alternative avenues for the exploration of topological electronic devices with fascinating functionalities.

ACKNOWLEDGMENTS

This work is supported by the National Natural Science Foundation of China (Grants No. 92165201, No. 11974324, No. U1832151, and No. 11804326), the Strategic Priority Research Program of Chinese Academy of Sciences (Grant No. XDC07010000), the Anhui Initiative in Quantum Information Technologies (Grant No. AHY170000), the Hefei Science Center CAS (Grant No. 2020HSC-UE014), and the Fundamental Research Funds for the Central Universities (Grant No. WK3510000013). Part of this work was carried out at the USTC Center for Micro and Nanoscale Research and Fabrication.

[1] S. A. Wolf, D. D. Awschalom, R. A. Buhrman, J. M. Daughton, S. von Molnár, M. L. Roukes, A. Y. Chtchelkanova, and D. M. Treger, Spintronics: A spin-based electronics vision for the future, Science **294**, 1488 (2001).

[2] D. D. Awschalom and M. E. Flatté, Challenges for semiconductor spintronics, Nat. Phys. **3**, 153 (2007).

[3] X. D. Xu, W. Yao, D. Xiao, and T. F. Heinz, Spin and pseudospins in layered transition metal dichalcogenides, Nat. Phys. **10**, 343 (2014).

[4] J. R. Schaibley, H. Y. Yu, G. Clark, P. Rivera, J. S. Ross, K. L. Seyler, W. Yao, and X. D. Xu, Valleytronics in 2D materials, Nat. Rev. Mater. **1**, 16055 (2016).

[5] X. G. Wan, A. M. Turner, A. Vishwanath, and S. Y. Savrasov, Topological semimetal and Fermi-arc surface states in the electronic structure of pyrochlore iridates, Phys. Rev. B **83**, 205101 (2011).

[6] H. M. Weng, C. Fang, Z. Fang, B. A. Bernevig, and X. Dai, Weyl semimetal phase in noncentrosymmetric transition-metal monophosphides, Phys. Rev. X **5**, 011029 (2015).

[7] N. P. Armitage, E. J. Mele, and A. Vishwanath, Weyl and Dirac semimetals in three-dimensional solids, Rev. Mod. Phys. **90**, 015001 (2018).

[8] D. T. Son and B. Z. Spivak, Chiral anomaly and classical negative magnetoresistance of Weyl metals, Phys. Rev. B **88**, 104412 (2013).

[9] X. C. Huang, L. X. Zhao, Y. J. Long, P. P. Wang, D. Chen, Z. H. Yang, H. Liang, M. Q. Xue, H. M. Weng, Z. Fang, X. Dai, and G. F. Chen, Observation of the chiral-anomaly-induced negative magnetoresistance in 3D Weyl semimetal TaAs, Phys. Rev. X **5**, 031023 (2015).

[10] S. Nandy, G. Sharma, A. Taraphder, and S. Tewari, Chiral Anomaly as the Origin of the Planar Hall Effect in Weyl Semimetals, Phys. Rev. Lett. **119**, 176804 (2017).

[11] N. Kumar, S. N. Guin, C. Felser, and C. Shekhar, Planar Hall effect in the Weyl semimetal GdPtBi, Phys. Rev. B **98**, 041103(R) (2018).

[12] Q. Ma, S. Y. Xu, C. K. Chan, C. L. Zhang, G. Q. Chang, Y. X. Lin, W. W. Xie, T. Palacios, H. Lin, S. Jia, P. A. Lee, P. Jarillo-Herrero, and N. Gedik, Direct optical detection of Weyl fermion chirality in a topological semimetal, Nat. Phys. **13**, 842 (2017).

[13] J. Ma, Q. Gu, Y. Liu, J. Lai, P. Yu, X. Zhuo, Z. Liu, J. H. Chen, J. Feng, and D. Sun, Nonlinear photoresponse of type-II Weyl semimetals, Nat. Mater. **18**, 476 (2019).

[14] N. Zhang, G. Zhao, L. Li, P. Wang, L. Xie, B. Cheng, H. Li, Z. Lin, C. Xi, J. Ke, M. Yang, J. He, Z. Sun, Z. Wang, Z. Zhang, and C. Zeng, Magnetotransport signatures of Weyl physics and discrete scale invariance in the elemental semiconductor tellurium, Proc. Natl. Acad. Sci. USA **117**, 11337 (2020).

[15] M. Hirayama, R. Okugawa, S. Ishibashi, S. Murakami, and T. Miyake, Weyl Node and Spin Texture in Trigonal Tellurium and Selenium, Phys. Rev. Lett. **114**, 206401 (2015).

[16] K. Nakayama, M. Kuno, K. Yamauchi, S. Souma, K. Sugawara, T. Oguchi, T. Sato, and T. Takahashi, Band splitting and Weyl nodes in trigonal tellurium studied by angle-resolved photoemission spectroscopy and density functional theory, Phys. Rev. B **95**, 125204 (2017).

[17] T. Ideue, M. Hirayama, H. Taiko, T. Takahashi, M. Murase, T. Miyake, S. Murakami, T. Sasagawa, and Y. Iwasa, Pressure-induced topological phase transition in noncentrosymmetric elemental tellurium, Proc. Natl. Acad. Sci. USA **116**, 25530 (2019).

[18] G. Qiu, C. Niu, Y. Wang, M. Si, Z. Zhang, W. Wu, and P. D. Ye, Quantum Hall effect of Weyl fermions in n-type semiconducting tellurene, Nat. Nanotechnol. **15**, 585 (2020).

[19] V. B. Anzin, M. I. Eremets, Y. V. Kosichkin, A. I. Nadezhdinskii and A. M. Shirokov, Measurement of the energy gap in tellurium under pressure, Phys. Status Solidi A **42**, 385 (1977).

[20] See Supplemental Material at http://link.aps.org/supplemental/10.1103/PhysRevApplied.17.054044 for experimental and theoretical details as well as additional figures and discussions, which includes Refs. [43–54].

[21] N. Zhang, B. Cheng, H. Li, L. Li, and C. G. Zeng, Magneto-transport properties of thin flakes of Weyl semiconductor tellurium, Chin. Phys. B **30**, 087304 (2021).

[22] Y. X. Wang, G. Qiu, R. X. Wang, S. Y. Huang, Q. X. Wang, Y. Y. Liu, Y. C. Du, W. A. Goddard, M. J. Kim, X. F. Xu, P. D. Ye, and W. Z. Wu, Field-effect transistors made from solution-grown two-dimensional tellurene, Nat. Electron. **1**, 228 (2018).

[23] M. Amani, C. Tan, G. Zhang, C. Zhao, J. Bullock, X. Song, H. Kim, V. R. Shrestha, Y. Gao, K. B. Crozier, M. Scott, and A. Javey, Solution-synthesized high-mobility tellurium nanoflakes for short-wave infrared photodetectors, ACS Nano **12**, 7253 (2018).

[24] L. Li, Y. Yu, G. J. Ye, Q. Ge, X. Ou, H. Wu, D. Feng, X. H. Chen, and Y. Zhang, Black phosphorus field-effect transistors, Nat. Nanotechnol. **9**, 372 (2014).

[25] S. Hikami, A. I. Larkin, and Y. Nagaoka, Spin-orbit interaction and magnetoresistance in the two dimensional random system, Prog. Theor. Phys. **63**, 707 (1980).

[26] M. Hirschberger, S. Kushwaha, Z. Wang, Q. Gibson, S. Liang, C. A. Belvin, B. A. Bernevig, R. J. Cava, and N. P. Ong, The chiral anomaly and thermopower of Weyl fermions in the half-Heusler GdPtBi, Nat. Mater. **15**, 1161 (2016).

[27] C. L. Zhang, *et al.*, Signatures of the Adler-Bell-Jackiw chiral anomaly in a Weyl fermion semimetal, Nat. Commun. **7**, 10735 (2016).

[28] C. Y. Guo, F. Wu, Z. Z. Wu, M. Smidman, C. Cao, A. Bostwick, C. Jozwiak, E. Rotenberg, Y. Liu, F. Steglich, and H. Q. Yuan, Evidence for Weyl fermions in a canonical heavy-fermion semimetal YbPtBi, Nat. Commun. **9**, 4622 (2018).

[29] E. Liu, *et al.*, Giant anomalous Hall effect in a ferromagnetic kagome-lattice semimetal, Nat. Phys. **14**, 1125 (2018).

[30] S. Jia, S. Y. Xu, and M. Z. Hasan, Weyl semimetals, Fermi arcs and chiral anomalies, Nat. Mater. **15**, 1140 (2016).

[31] Q. Li, D. E. Kharzeev, C. Zhang, Y. Huang, I. Pletikosić, A. V. Fedorov, R. D. Zhong, J. A. Schneeloch, G. D. Gu, and T. Valla, Chiral magnetic effect in $ZrTe_5$, Nat. Phys. **12**, 550 (2016).

[32] G. Long, D. Maryenko, J. Shen, S. Xu, J. Hou, Z. Wu, W. K. Wong, T. Han, J. Lin, Y. Cai, R. Lortz, and N. Wang, Achieving ultrahigh carrier mobility in two-dimensional hole gas of black phosphorus, Nano Lett. **16**, 7768 (2016).

[33] Z. Yu, Z. Y. Ong, Y. Pan, Y. Cui, R. Xin, Y. Shi, B. Wang, Y. Wu, T. Chen, Y. W. Zhang, G. Zhang, and X. Wang, Realization of room-temperature phonon-limited carrier

transport in monolayer MoS_2 by dielectric and carrier screening, Adv. Mater. **28**, 547 (2016).

[34] J. Liu, T. H. Hsieh, P. Wei, W. Duan, J. Moodera, and L. Fu, Spin-filtered edge states with an electrically tunable gap in a two-dimensional topological crystalline insulator, Nat. Mater. **13**, 178 (2014).

[35] X. Qian, J. Liu, L. Fu, and J. Li, Quantum spin Hall effect in two-dimensional transition metal dichalcogenides, Science **346**, 1344 (2014).

[36] W. G. Vandenberghe and M. V. Fischetti, Imperfect two-dimensional topological insulator field-effect transistors, Nat. Commun. **8**, 14184 (2017).

[37] Y. Xu, Y.-R. Chen, J. Wang, J.-F. Liu, and Z. Ma, Quantized Field-Effect Tunneling between Topological Edge or Interface States, Phys. Rev. Lett. **123**, 206801 (2019).

[38] J. L. Collins, A. Tadich, W. Wu, L. C. Gomes, J. N. B. Rodrigues, C. Liu, J. Hellerstedt, H. Ryu, S. Tang, S. K. Mo, S. Adam, S. A. Yang, M. S. Fuhrer, and M. T. Edmonds, Electric-field-tuned topological phase transition in ultrathin Na_3Bi, Nature **564**, 390 (2018).

[39] M. M. Vazifeh and M. Franz, Electromagnetic Response of Weyl Semimetals, Phys. Rev. Lett. **111**, 027201 (2013).

[40] H. Wang, H. Liu, Y. Li, Y. Liu, J. Wang, J. Liu, J. Y. Dai, Y. Wang, L. Li, J. Yan, D. Mandrus, X. C. Xie, and J. Wang, Discovery of log-periodic oscillations in ultraquantum topological materials, Sci. Adv. **4**, eaau5096 (2018).

[41] S. Nakatsuji, N. Kiyohara, and T. Higo, Large anomalous Hall effect in a non-collinear antiferromagnet at room temperature, Nature **527**, 212 (2015).

[42] T. Liang, J. Lin, Q. Gibson, S. Kushwaha, M. Liu, W. Wang, H. Xiong, J. A. Sobota, M. Hashimoto, P. S. Kirchmann, Z.-X. Shen, R. J. Cava, and N. P. Ong, Anomalous Hall effect in $ZrTe_5$, Nat. Phys. **14**, 451 (2018).

[43] R. M. Martin, G. Lucovsky, and K. Helliwell, Intermolecular bonding and lattice dynamics of Se and Te, Phys. Rev. B **13**, 1383 (1976).

[44] H. Yamada and S. Takada, Negative magnetoresistance of ferromagnetic metals due to spin fluctuations, Prog. Theor. Phys. **48**, 1828 (1972).

[45] N. P. Ong and S. Liang, Experimental signatures of the chiral anomaly in Dirac-Weyl semimetals, Nat. Rev. Phys. **3**, 394 (2021).

[46] S. Liang, J. Lin, S. Kushwaha, J. Xing, N. Ni, R. J. Cava, and N. P. Ong, Experimental tests of the chiral anomaly magnetoresistance in the Dirac-Weyl semimetals Na_3Bi and GdPtBi, Phys. Rev. X **8**, 031002 (2018).

[47] R. D. dos Reis, M. O. Ajeesh, N. Kumar, F. Arnold, C. Shekhar, M. Naumann, M. Schmidt, M. Nicklas, and E. Hassinger, On the search for the chiral anomaly in Weyl semimetals: The negative longitudinal magnetoresistance, New J. Phys. **18**, 085006 (2016).

[48] P. N. Argyres and E. N. Adams, Longitudinal magnetoresistance in the quantum limit, Phys. Rev. **104**, 900 (1956).

[49] P. Goswami, J. H. Pixley, and S. Das Sarma, Axial anomaly and longitudinal magnetoresistance of a generic three-dimensional metal, Phys. Rev. B **92**, 075205 (2015).

[50] H. Li, H. He, H.-Z. Lu, H Zhang, H. Liu, R. Ma, Z. Fan, S.-Q. Shen, and J. Wang, Negative magnetoresistance in Dirac semimetal Cd_3As_2, Nat. Commun. **7**, 10301 (2016).

[51] A. A. Burkov, Giant planar Hall effect in topological metals, Phys. Rev. B **96**, 041110(R) (2017).

[52] H. Li, H.-W. Wang, H. He, J. Wang, and S.-Q. Shen, Giant anisotropic magnetoresistance and planar Hall effect in the Dirac semimetal Cd_3As_2, Phys. Rev. B **97**, 201110(R) (2018).

[53] F. Chen, X. Luo, J. Yan, Y. Sun, H. Lv, W. Lu, C. Xi, P. Tong, Z. Sheng, X. Zhu, W. Song, and Y. Sun, Planar Hall effect in the type-II Weyl semimetal T_d-$MoTe_2$, Phys. Rev. B **98**, 041114(R) (2018).

[54] P. Li, C. Zhang, Y. Wen, L. Cheng, G. Nichols, D. G. Cory, G.-X. Miao, and X.-X. Zhang, Anisotropic planar Hall effect in the type-II topological Weyl semimetal WTe_2, Phys. Rev. B **100**, 205128 (2019).